Since January 2020 Elsevier has created a COVID-19 resource centre with free information in English and Mandarin on the novel coronavirus COVID-19. The COVID-19 resource centre is hosted on Elsevier Connect, the company's public news and information website.

The American Journal of Pathology, Vol. 193, No. 6, June 2023

ELSEVIER

The American Journal of
PATHOLOGY
ajp.amjpathol.org

ANIMAL MODELS

Severe Acute Respiratory Syndrome Coronavirus 2 Vasculopathy in a Syrian Golden Hamster Model

Erin E. Ball,*† Christopher M. Weiss,* Hongwei Liu,* Kenneth Jackson,* M. Kevin Keel,* Christopher J. Miller,‡§ Koen K.A. Van Rompay,*‡ Lark L. Coffey,* and Patricia A. Pesavento*

From the Department of Pathology, Microbiology, and Immunology, the California National Primate Center,‡ and the Center for Immunology and Infectious Diseases,§ University of California, Davis, California; and the US Army Veterinary Corps,† Washington, District of Columbia*

Accepted for publication February 13, 2023.

Address correspondence to Lark L. Coffey, Ph.D., Department of Pathology, Microbiology, and Immunology, School of Veterinary Medicine, University of California, Davis, 1 Shields Ave., Bldg. VM3A, Davis, CA 95616.
E-mail: lcoffey@ucdavis.edu.

Clinical evidence of vascular dysfunction and hypercoagulability as well as pulmonary vascular damage and microthrombosis are frequently reported in severe cases of human coronavirus disease 2019 (COVID-19). Syrian golden hamsters recapitulate histopathologic pulmonary vascular lesions reported in patients with COVID-19. Herein, special staining techniques and transmission electron microscopy further define vascular pathologies in a Syrian golden hamster model of human COVID-19. The results show that regions of active pulmonary inflammation in severe acute respiratory syndrome coronavirus 2 (SARS-CoV-2) infection are characterized by ultrastructural evidence of endothelial damage with platelet marginalization and both perivascular and subendothelial macrophage infiltration. SARS-CoV-2 antigen/RNA was not detectable within affected blood vessels. Taken together, these findings suggest that the prominent microscopic vascular lesions in SARS-CoV-2–inoculated hamsters likely occur due to endothelial damage followed by platelet and macrophage infiltration. *(Am J Pathol 2023, 193: 690–701; https://doi.org/10.1016/j.ajpath.2023.02.013)*

Severe acute respiratory syndrome coronavirus 2 (SARS-CoV-2) infection in humans varies from asymptomatic to severe respiratory disease, progressing to acute respiratory distress syndrome, multiorgan dysfunction, and death in a subset of patients. As the pandemic has progressed, there have been increasing reports documenting clinical evidence of coagulation abnormalities (coagulopathy) and microscopic indicators of pulmonary vascular damage (vasculopathy), including endotheliitis, defined as subendothelial leukocyte infiltration with lifting and/or damage to endothelial cells,[1] vasculitis, and microthrombosis associated with severe cases of coronavirus disease 2019 (COVID-19).[2–5] Syrian golden hamsters (*Mesocricetus auratus*) are naturally susceptible to SARS-CoV-2 and closely recapitulate the clinical, virological, and histopathologic features of human COVID-19.[6–11] Herein, a Syrian golden hamster model was used to define SARS-CoV-2–induced vasculopathies, which have not been fully characterized in this animal model. Hamsters show regions of active SARS-CoV-2–induced pulmonary inflammation that exhibit ultrastructural evidence of endothelial damage with detachment from the underlying basement membrane, platelet marginalization, and marked perivascular and subendothelial mononuclear inflammation composed primarily of macrophages. At 3 to 6 or 7 days post inoculation (dpi), SARS-CoV-2 antigen/RNA was not detectable within affected blood vessels. These findings suggest that the microscopic vascular lesions in SARS-CoV-2–inoculated hamsters occur not primarily due to direct viral infection of the endothelium, but rather due to indirect endothelial

Supported by the Center for Immunology and Infectious Diseases, University of California, Davis, intramural funding (C.J.M.); NIH grant R01-AI118590 (C.J.M.); the Graduate Student Support Program, University of California, Davis (E.E.B.); and the US Army Medical Center of Excellence Long Term Health Education and Training Program (E.E.B.).

Disclosures: None declared.

Current address of E.E.B., Armed Forces Research Institute of Medical Sciences, Bangkok, Thailand; of C.M.W., MRI Global, Kansas City, MO.

https://doi.org/10.1016/j.ajpath.2023.02.013

damage with loss of endothelial attachment and vascular compromise followed by platelet and macrophage infiltration.

Materials and Methods

Hamsters, Viral Inoculation, and Euthanasia

All hamster experiments were conducted under protocol number 21868, approved by the University of California, Davis, Institutional Animal Care and Use Committee. Infectious virus was handled in certified animal biosafety level 3 laboratory spaces in compliance with approved institutional biological use authorization number R2813. University of California, Davis, is accredited by the Association for Assessment and Accreditation of Laboratory Animal Care, and all work adhered to the NIH *Guide for the Care and Use of Laboratory Animals*.[12] Two experiments, each using 8- to 10-week–old male and female Syrian golden hamsters, were performed [experiment 1, $N = 15$ (8 males and 7 females); experiment 2, $N = 8$ (4 males and 4 females)]; the animals were from Charles River Laboratories (Wilmington, MA) and were acclimated for up to 7 days at 22°C to 25°C and a 12:12-hours light/dark cycle. Rodent chow with 18% protein content and sterile bottled water were provided *ad libitum* for the duration of the experiment.

SARS-CoV-2/human/USA/CA-CZB-59X002/2020 (GenBank, *https://www.ncbi.nlm.nih.gov/nuccore/MT394528*; accession number MT394528, data available to public) from a 2020 patient with COVID-19 in Northern California was passaged twice in Vero-E6 (ATCC, Manassas, VA) cells to achieve a titer of 2.2×10^7 plaque-forming units (PFUs)/mL and stored at −80°C. Randomly selected hamsters from experiment 1 and experiment 2 were anesthetized with isoflurane and administered 30 μL of phosphate-buffered saline (PBS; Thermo Fisher Scientific, Waltham, MA) [experiment 1, $N = 4$ (2 males and 2 females); experiment 2, $N = 2$ (1 male and 1 female)] or SARS-CoV-2 diluted in PBS at a dose of 10^4 PFUs [experiment 1, $N = 11$ (6 males and 5 females); experiment 2, $N = 6$ (3 males and 3 females)] intranasally by a hanging drop over both nares. Hamsters were monitored daily for clinical signs through the experimental end point and euthanized if weight loss exceeded 20% or if they appeared moribund. Hamsters were anesthetized daily with isoflurane, weighed, and throat swabbed (Puritan; Thermo Fisher Scientific). Swabs were vortexed in 400 μL of Dulbecco's modified Eagle's medium (Thermo Fisher Scientific) and stored at −80°C. Before euthanasia, whole blood was collected via submandibular vein puncture, allowed to clot at room temperature for >10 minutes, and centrifuged for 5 minutes at 8000 × *g*. Serum was also stored at −80°C. Following humane euthanasia by isoflurane overdose and cervical dislocation, hamsters were perfused with cold sterile PBS, and a necropsy was performed. Tissues were divided and processed for virology assays and histopathology. Lung was homogenized in 1 to 10 μL/mg Dulbecco's modified Eagle's medium with a sterile glass bead using a TissueLyser (Qiagen, Germantown, MD) at 30 Hz for 4 minutes, centrifuged at 10,000 × *g* for 5 minutes, and stored at −80°C.

Plaque Assays

Infectious SARS-CoV-2 was detected from thawed hamster samples and remaining inocula immediately after inoculation using Vero cell plaque assays. Briefly, samples were serially diluted 10-fold in Dulbecco's modified Eagle's medium with 1% bovine serum albumin (both from Thermo Fisher Scientific) starting at an initial dilution of 1:8. The 12-well plates of confluent Vero CCL-81 cells (ATCC) were inoculated with 125 μL of each dilution and incubated at 37°C and 5% CO_2 for 1 hour. After incubation, each cell monolayer was overlaid with 0.5% agarose (Invitrogen, Carlsbad, CA) diluted in Dulbecco's modified Eagle's medium with 5% fetal bovine serum and 1× antibiotic-antimycotic (both from Thermo Fisher Scientific) and incubated for 3 days at 5% CO_2 and 37°C. Cell monolayers were then fixed with 4% formalin for 30 minutes, agar plugs were gently removed, and viable cells were stained for 10 minutes with 0.05% crystal violet (Sigma, St. Louis, MO) in 20% ethanol, then rinsed with water. Plaques were counted and viral titers were recorded as the reciprocal of the highest dilution where plaques were noted (PFUs per swab, mg tissue, or mL inoculum).

Necropsy Tissue Processing and Histopathology

At necropsy, lung was inflated, and tissues were fixed for 48 hours at room temperature with a 10-fold volume of 10% neutral-buffered formalin (Thermo Fisher Scientific). A subset of tissues, including lung, brain, liver, spleen, heart, peripheral lymph nodes, eye, and nasal cavity, was embedded in paraffin, thin sectioned (4 μm thick), and stained routinely with hematoxylin and eosin. Hematoxylin and eosin–stained slides were scanned to ×40 magnification using an Aperio slide scanner (Leica Biosystems, Deer Park, IL) with a magnification doubler and a resolution of 0.25 μm/pixel. Image files were uploaded on a Leica hosted web-based site, and a board-certified veterinary anatomic pathologist (E.E.B.) blindly evaluated sections for SARS-CoV-2–induced histologic lesions. For immunofluorescence, fixed tissue was cryoprotected by rinsing overnight in PBS at 4°C, followed by transfer into 30% sucrose (Thermo Fisher Scientific) in 1× PBS for a second night, frozen over dry ice in Andwin Scientific Tissue-Tek cryomolds filled with Tissue-plus OCT compound, wrapped in parafilm (all from Thermo Fisher Scientific), and stored at −20°C.

In Situ Hybridization

Colorimetric *in situ* hybridization was performed according to the manufacturer's instructions, using the RNAscope 2.5 HD Red Reagent Kit (Advanced Cell Diagnostics, Newark,

CA) and RNAscope Probe - V-nCoV2019-S (Advanced Cell Diagnostics; catalog number 526 848,561). RNAscope Negative Control Probe - DapB (Advanced Cell Diagnostics; catalog number 310043) and lung tissue from a SARS-CoV-2−uninfected control animal hybridized with the SARS-CoV-2 probes served as negative controls. RNAscope Probe-Mau-Ppib (Advanced Cell Diagnostics; catalog number 890851) served as a positive control. Briefly, each deparaffinized section (5 μm thick) was pretreated with 1× Target Retrieval Buffer (Abcam, Eugene, OR) at 100°C for 15 minutes and Protease Plus (Advanced Cell Diagnostics) at 40°C for 30 minutes before hybridization at 40°C for 2 hours. This was followed by a cascade of signal amplification and signal detection using a Fast Red solution for 10 minutes at room temperature. Slides were counterstained with hematoxylin, dehydrated, coverslipped, and scanned to ×40 magnification, as described above. Positive cells (defined as those exhibiting red cytoplasmic staining) were identified on the basis of location and cell morphology.

Immunohistochemistry

Slides were deparaffinized in xylene and 100% ethanol. Endogenous peroxidases were blocked by placing slides in 3% hydrogen peroxide in methanol (all from Thermo Fisher Scientific) for 30 minutes. After rehydration, ionized calcium-binding adaptor molecule 1 (Iba1), CD3, and CD79a slides underwent heat-induced antigen retrieval for 30 minutes using distilled water (Iba1) or citrate solution (CD3 and CD79a) composed of 20 mL 10× stock solution [12.9 g citric acid, trisodium salt, anhydrous, 500 mL distilled water, 10 mL 1N hydrogen chloride to adjust pH to 6.1, and 2.5 mL Tween 20 (all from Thermo Fisher Scientific)] and 180 mL deionized water. von Willebrand factor slides were incubated for 10 minutes with proteinase K (Agilent Dako, Santa Clara, CA; catalog number S3020). Following antigen retrieval, all slides were blocked for 20 minutes in 20 mL normal horse serum (Vector Laboratories, Burlingame, CA) diluted in 180 mL PBS. Antibodies used for immunohistochemistry were as follows: rabbit polyclonal anti-Iba1 at 1:600 dilution (Wako Chemicals, Richmond, VA; catalog number 19-19741); anti-rat CD3 clone CD3-12 at 1:10 dilution (supplied by Dr. Peter Moore, University of California, Davis); mouse anti-human CD79a clone HM57 at 1:100 dilution (Bio Rad, Hercules, CA; catalog number MCA2538H); and rabbit polyclonal anti−von Willebrand factor at 1:2000 dilution (Agilent Dako; catalog number A0082). Slides were incubated with primary antibodies at room temperature for 1 hour with gentle agitation, then allowed to incubate at room temperature for 30 minutes with rat-on-canine (CD3), mouse-on-canine (CD79a), or rabbit-on-canine (Iba1 and von Willebrand factor) horseradish peroxidase−polymer (all from BioCare Medical, Pacheco, CA). Colorimetric detection was performed according to manufacturer's instructions using Vector NovaRED peroxidase substrate kit (Vector Laboratories), and slides were counterstained with hematoxylin and bluing reagent (both from Thermo Fisher Scientific) before mounting.

Immunofluorescence

Glass slides with sections (12 μm thick) of frozen, cryoprotected lung tissue cut with a Leica CM1860 cryotome (Leica Biosystems) were blocked in 2% bovine serum albumin, 0.3% Triton X-100 (Thermo Fisher Scientific), and 10% normal donkey serum (Jackson Laboratories, West Grove, PA) in 1× PBS for 1 hour at room temperature. Slides were incubated overnight with primary antibodies at 4°C: mouse anti-pan cytokeratin (Lu5) at 1:100 dilution (BioCare Medical; catalog number CM043C); mouse anti-CD31/platelet endothelial cell adhesion molecule 1 antibody (JC/70A) at 1:20 dilution (Novus Biologicals, Littleton, CO; catalog number NB600-562); rat anti-mouse CD41 (MWReg30) at 1:100 dilution (BD Pharmingen, Franklin Lakes, NJ; catalog number 553847); mouse anti-human CD61 (Y2/51) at 1:50 dilution (Bio Rad; catalog number MCA2588); and rabbit polyclonal anti-SARS2 nucleocapsid protein at 1:10,000 dilution (Sino Biologicals, Waye, PA; catalog number 40143-R019). Slides were incubated with secondary antibodies, including donkey anti-rabbit AF-594 (Invitrogen, Waltham, MA; catalog number A21207), donkey anti-mouse AF-488 (Invitrogen; catalog number A21202), and goat anti-rat AF-488 (Invitrogen; catalog number A48262), diluted 1:250 in PBS + 10% donkey serum for 1 hour, and mounted using prolong Gold antifade with DAPI (Thermo Fisher Scientific; catalog number P36931). Z-stacks in a 1.04-μm step size were acquired on a Leica SP8 STED 3× confocal microscope controlled by Leica LAS X software with a 20×/0.75-mm HC PL APO CS2 objective. Images were processed using ImageJ Fiji version 13.0.6 (NIH, Bethesda, MD; *https://imagej.net/software/fiji*, last accessed December 22, 2022).

Transmission Electron Microscopy

Lung tissues from two experiment 1 SARS-CoV-2−inoculated hamsters (one each at 3 dpi and 6 dpi) and two experiment 2 SARS-CoV-2−inoculated hamsters (one each at 3 dpi and 6 dpi) were evaluated by transmission electron microscopy (TEM). After fixation in 2.5% glutaraldehyde and 2% paraformaldehyde (both from Ted Pella, Redding, CA) in 0.1 mol/L sodium phosphate buffer (Thermo Fisher Scientific), tissues were post-fixed in 1% osmium tetroxide [Electron Microscopy Sciences (EMS), Hatfield, PA] in 0.1 mol/L sodium phosphate buffer for 1 hour, dehydrated for 30 minutes each in 50%, 75%, and 95% ethanol, dehydrated twice for 20 minutes in 100% ethanol, and placed in propylene oxide (EMS) twice for 15 minutes. Samples were pre-infiltrated overnight in a 1:1 ratio of propylene oxide/resin [composed of 450 mL

dodecenyl succinic anhydride, 250 mL araldite 6005 (both from EMS), 82.5 mL Epon 812 (Polysciences Inc., Warrington, PA), 12.5 mL dibutyl phthalate (Ted Pella), and 450 μL benzyldimethylamine (EMS)]. The following day, tissues were infiltrated in 100% resin for 5 hours, embedded with fresh resin, and polymerized at 60°C overnight. Embedded tissues were sectioned with a Leica EM UC6 ultramicrotome (Leica Biosystems) at a thickness of 90 nm, collected on copper mesh grids (EMS), and stained with 4% aqueous uranyl acetate for 20 minutes and 0.2% lead citrate for 2 minutes (both from Ted Pella) in 0.1N NaOH (Thermo Fisher Scientific). TEM imaging was done on FEI Talos L120C at 80 kV using a Ceta-M 16 MP camera (Thermo Fisher Scientific). For each hamster, two lung sections were examined. The images shown are from experiment 1 and 2 hamsters and are representative of changes in all SARS-CoV-2–inoculated hamsters evaluated.

Results

Validation of the Model

The experimental design is summarized in Supplemental Figure S1A. Briefly, two groups of hamsters (experiment 1, $N = 11$; experiment 2, $N = 6$) were inoculated intranasally with SARS-CoV-2 Alpha (B.1.1.7) or mock inoculated (experiment 1, $N = 4$; experiment 2, $N = 2$) with Dulbecco's PBS on day 0, monitored daily for weight loss and clinical disease and to swab the oropharyngeal cavity, and euthanized on 3, 6, or 7 dpi. A dose of 10^4 PFUs was chosen because previous studies modeling human COVID-19 in Syrian golden hamsters have shown that SARS-CoV-2 inoculum doses ranging from 10^3 to $10^{5.6}$ PFUs reproducibly infect all animals and produce similar infectious lung and tracheal titers and lung and spleen inflammation scores.[6–9,13,14] Herein, SARS-CoV-2–inoculated hamsters from experiments 1 and 2 showed similar trends in body weight and recovery of infectious virus from the respiratory tract. A subset of experiment 1 and 2 hamsters inoculated with SARS-CoV-2 exhibited mild weight loss from 2 to 3 dpi (Supplemental Figure S1B), although none reached euthanasia criteria (loss of 20% of day 0 weight) or displayed clinical signs of illness. In both experiments, infectious virus was recovered from the upper respiratory tract between 1 and 3 dpi and from the lung at 3 dpi (Supplemental Figure S1, C and D). Most hamsters did not become viremic, although infectious virus was detected in the plasma of one female hamster from experiment 1, which also had a low infectious virus titer in the duodenum at 3 dpi. Otherwise, infectious virus was not detected in other hamster tissues. Overall, SARS-CoV-2–inoculated hamsters developed nonlethal infection with infectious virus recoverable until 3 dpi from the upper airway and lung. All hamsters inoculated with SARS-CoV-2 developed moderate to severe microscopic pulmonary lesions (Figure 1). No significant microscopic abnormalities were noted in the brain, heart, spleen, liver, gastrointestinal tract, kidneys, or male/female reproductive tissues of any examined hamster. Inoculation of additional hamsters with emerging SARS-CoV-2 variants, including Delta (B.1.617.2) and Epsilon (B.1.427 and B.1.429) variants, produced similar histopathologic lesions and is described elsewhere.[15,16]

Syrian Golden Hamsters Inoculated with SARS-CoV-2 Develop Progressive Broncho-Interstitial Pneumonia with Prominent Vascular Lesions

SARS-CoV-2–induced airway disease and pneumonia in two independent experimental groups of hamsters were assessed using two methods. First, ImageJ was used to quantify the approximate lung surface area exhibiting microscopic lesions consistent with COVID-19 (defined as inflammation, necrosis, hemorrhage, and/or edema visible at subgross magnification) as a proxy for the overall extent and severity of pulmonary lesions. Next, pathologic lesions specifically affecting pulmonary vasculature were scored according to the criteria outlined in Supplemental Table S1. Both scores were significantly higher in SARS-CoV-2–inoculated hamsters when compared with uninfected controls (Figure 1A). Experiment 1 and 2 SARS-CoV-2–inoculated hamsters exhibited a progressive increase in the extent and severity of lung lesions from 3 to 7 dpi (Figure 1). At 3 dpi, there was patchy neutrophilic and histiocytic inflammation centered on large airways (bronchitis and bronchiolitis), as well as variable bronchiolar epithelial and alveolar septal necrosis with replacement by fibrin, hemorrhage, edema, necrotic debris, numerous neutrophils, and macrophages, and scattered multinucleated syncytial cells (Figure 1C) that was absent from uninfected control hamsters (Figure 1B). By 6 dpi, lesions progressed to widespread necrotizing broncho-interstitial pneumonia (Figure 1D). Reparative changes, consisting of bronchiolar epithelial hyperplasia (Figure 1D) and type II pneumocyte hyperplasia, were also common by 6 dpi. Vascular lesions, including marked perivascular cuffing and subendothelial mononuclear inflammatory cell infiltration (endotheliitis) with variable transmigration of the vessel wall, were noted frequently at both time points (Figure 1, C and D); however, necrotizing vasculitis and thrombosis were not prominent features. These histologic features are consistent with published data from hamster models,[6–10] including lesions reported in association with emerging SARS-CoV-2 variants.[15,16]

Pulmonary Subendothelial Inflammation in SARS-CoV-2–Inoculated Hamsters Is Characterized by Endothelial Damage with Macrophage and Platelet Infiltration

Immunohistochemistry, immunofluorescence, *in situ* hybridization, and TEM were used to further characterize foci

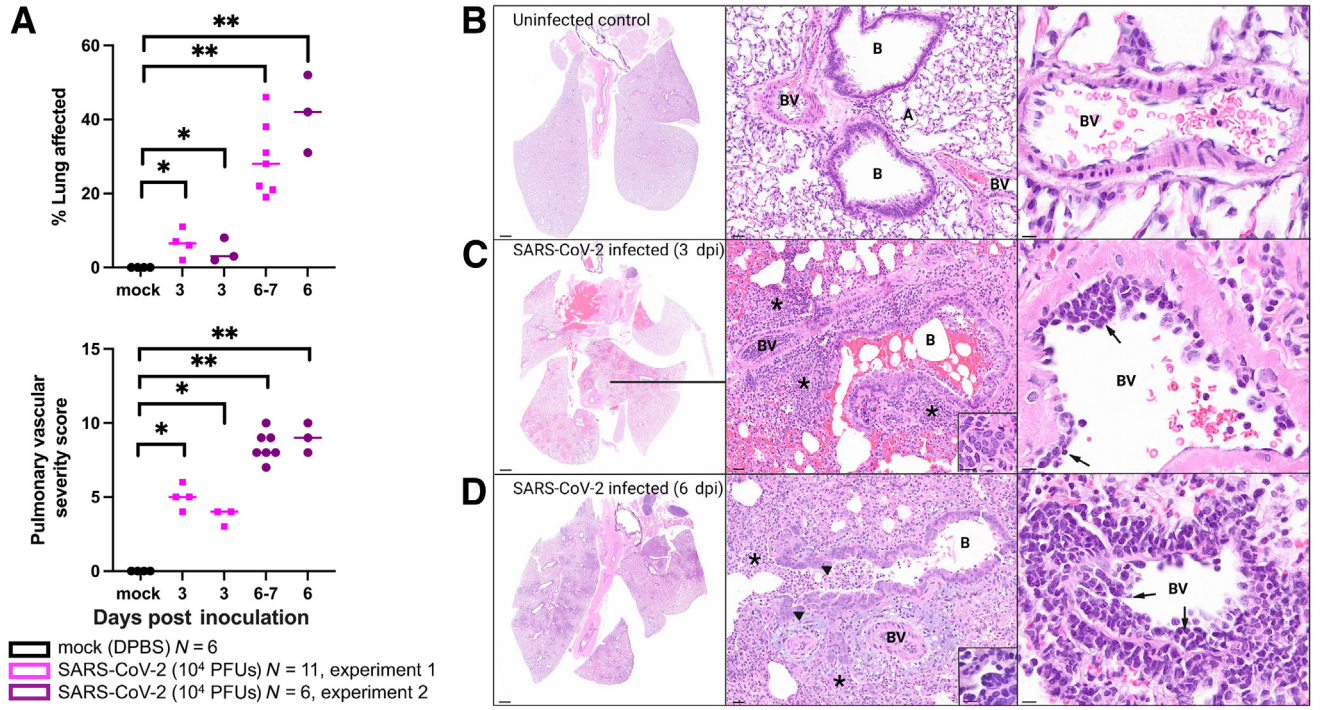

Figure 1 Combined pulmonary pathology severity score summary and photomicrographs of hematoxylin and eosin–stained lung sections from uninfected and SARS-CoV-2–inoculated hamsters at 3 and 6 days post inoculation (dpi). **A:** The proportion of lung surface area exhibiting SARS-CoV-2–induced microscopic lesions (**top panel**) and the mean pulmonary vascular histology severity score (**bottom panel**) increase from 3 to 7 dpi in group 1 and 2 SARS-CoV-2–inoculated hamsters. Scores are significantly higher in SARS-CoV-2–inoculated hamsters than in mock-inoculated control animals (*U*-test). **Horizontal lines** denote means. Each dot/square indicates an individual hamster. **B:** Normal lung from uninfected hamster. **C:** Lung from a SARS-CoV-2–inoculated hamster euthanized at 3 dpi. There is patchy necrohemorrhagic bronchiolitis and loss of normal alveolar septal architecture with replacement by hemorrhage, fibrin, and an inflammatory infiltrate (**asterisks**; **middle panel**) composed primarily of neutrophils and macrophages (not shown here but identifiable at higher magnification), with scattered multinucleated syncytial cells (**inset**; **middle panel**) and mononuclear endotheliitis (**arrows**; **right panel**) with perivascular inflammation. **D:** Lung from a SARS-CoV-2–inoculated hamster euthanized at 6 dpi. There is widespread broncho-interstitial pneumonia (**asterisks**; **middle panel**) with bronchiolar epithelial hyperplasia (**arrowheads**; **middle panel**) and multinucleated syncytial cells (**inset**; **middle panel**). **Right panel:** Endotheliitis (**arrows**) and perivascular inflammation remain prominent. $^{*}P \leq 0.05$, $^{**}P \leq 0.01$. Scale bars: 1 mm (**B–D**, **left panels**); 30 μm (**B–D**, **middle panels**); 20 μm (**B–D**, **right panels**); 10 μm (**C** and **D**, **insets**). A, alveolar septa; B, bronchiole; BV, blood vessel; DPBS, Dulbecco's phosphate-buffered saline; PFU, plaque-forming unit.

of endotheliitis identified on hematoxylin and eosin–stained slides. Immunohistochemistry staining with antibodies against von Willebrand factor/factor 8 (endothelial cells) (Figure 2A), Iba1 (macrophages), CD3 (T lymphocytes), and CD79a (B lymphocytes) revealed that, at 3, 6, and 7 dpi, the mononuclear cells adhered to the endothelial surface or infiltrating subendothelial vascular layers were consistent primarily with macrophages (Figure 2B). There were also low numbers of T lymphocytes (Figure 2C) and few B lymphocytes (Figure 2D). Internal immunohistochemistry controls are shown in Supplemental Figure S2.

Immunofluorescence antibodies against SARS-CoV-2 nucleocapsid protein demonstrated viral antigen in hamster terminal bronchiolar epithelium, type I pneumocytes, and, less commonly, alveolar macrophages at 3 dpi (Figure 3, A–C). Anti-endothelial cell antibody CD31 (green) highlighted endothelial cells lining a small pulmonary artery (Figure 3A). Green anti-platelet antibody (CD41) localized along the arteriolar endothelium (Figure 3B), indicating areas of platelet marginalization, which were not present in the mock-inoculated hamster. The presence of intracytoplasmic green signal within mononuclear cells (Figure 3, B and C) was consistent with platelet phagocytosis by macrophages. Viral nucleocapsid protein was not identified within or near blood vessels (Figure 3, A–C) or within a mock-inoculated hamster. *In situ* hybridization was used to assess the cellular tropism of SARS-CoV-2 in the hamster respiratory tract (Figure 3, D–L), where positive cells demonstrated intracytoplasmic red signal. Overall, SARS-CoV-2 RNA was observed primarily at 3 dpi (Figure 3) within bronchial/bronchiolar epithelial cells, type I and II pneumocytes, and (less frequently) alveolar macrophages, where it corresponded with areas of inflammation. Notably, viral RNA was not identified within or associated with the pulmonary vasculature (Figure 3, F, I, and L).

Ultrastructurally, there was evidence of endothelial activation and injury in the pulmonary vasculature of SARS-CoV-2–inoculated hamsters in both experimental replicates, particularly at 6 dpi. Activated endothelial cells bulged into the vascular lumen (Figure 4A), often with

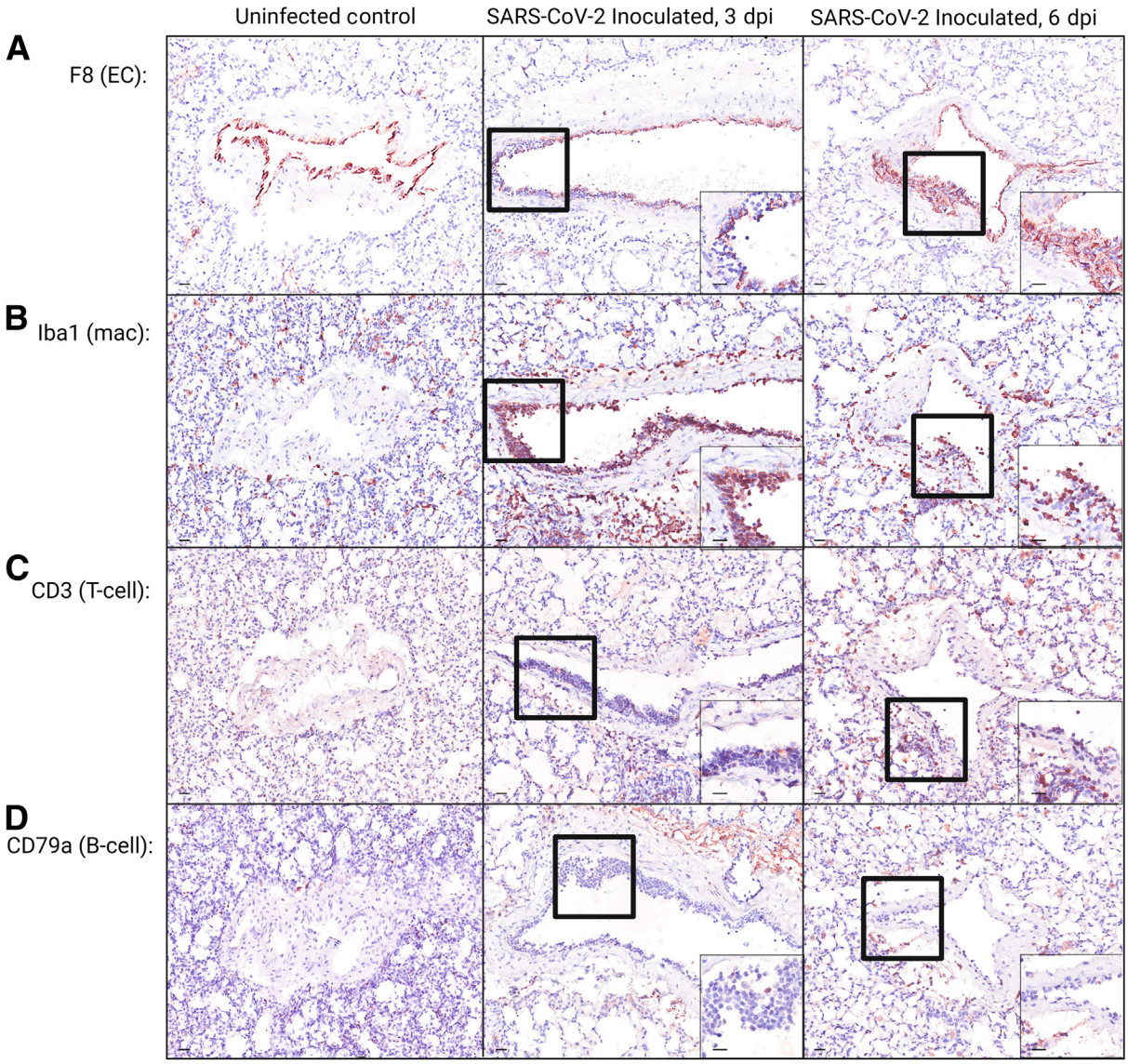

Figure 2 Photomicrographs of immunohistochemically (IHC) stained lung sections from uninfected and SARS-CoV-2—inoculated hamsters. **A**—**D:** IHC staining using antibodies against endothelial cells [ECs; von Willebrand factor/factor 8 (F8); **A**], macrophages [macs; ionized calcium-binding adaptor molecule 1 (Iba1); **B**], T lymphocytes (T-cells; CD3; **C**), and B lymphocytes (B-cells; CD79a; **D**), where positive cells exhibit intracytoplasmic or membranous brown staining. **A**—**D: Insets:** Higher-magnification views of the **black boxed areas.** Overall, IHC indicates that the subendothelial mononuclear cell infiltrate is composed primarily of macrophages. See Supplemental Figure S2 for internal controls. Scale bars = 20 μm (**A**—**D**). Dpi, days post inoculation.

irregular, frond-like filopodia (Figure 4B), and thickened, irregular basal laminae (Figure 4C). Damaged, degenerating endothelial cells exhibited cytoplasmic vacuolation with partial detachment from the basal lamina (Figure 4, C and D). Mononuclear cells were present within resulting subendothelial spaces (Figure 4A). These features were corroborated by the corresponding light microscopic images (Figure 4, E and F), which also exhibited endothelial bulging into the lumen and subintimal infiltration of mononuclear cells (Figure 4C) with endothelial cytoplasmic vacuolation (Figure 4E). There were no viral particles noted within or associated with affected endothelial cells. Taken together, these results are suggestive of vascular endothelial damage with mononuclear subendothelial inflammation and infiltration of platelets into areas of active pulmonary infection and inflammation.

Discussion

The histopathologic pulmonary lesions reported here, including moderate to severe broncho-interstitial pneumonia and alveolar damage with prominent perivascular and subendothelial inflammation, are comparable with the limited published autopsy data available from patients with severe COVID-19,[2,17–19] although hyaline membranes and

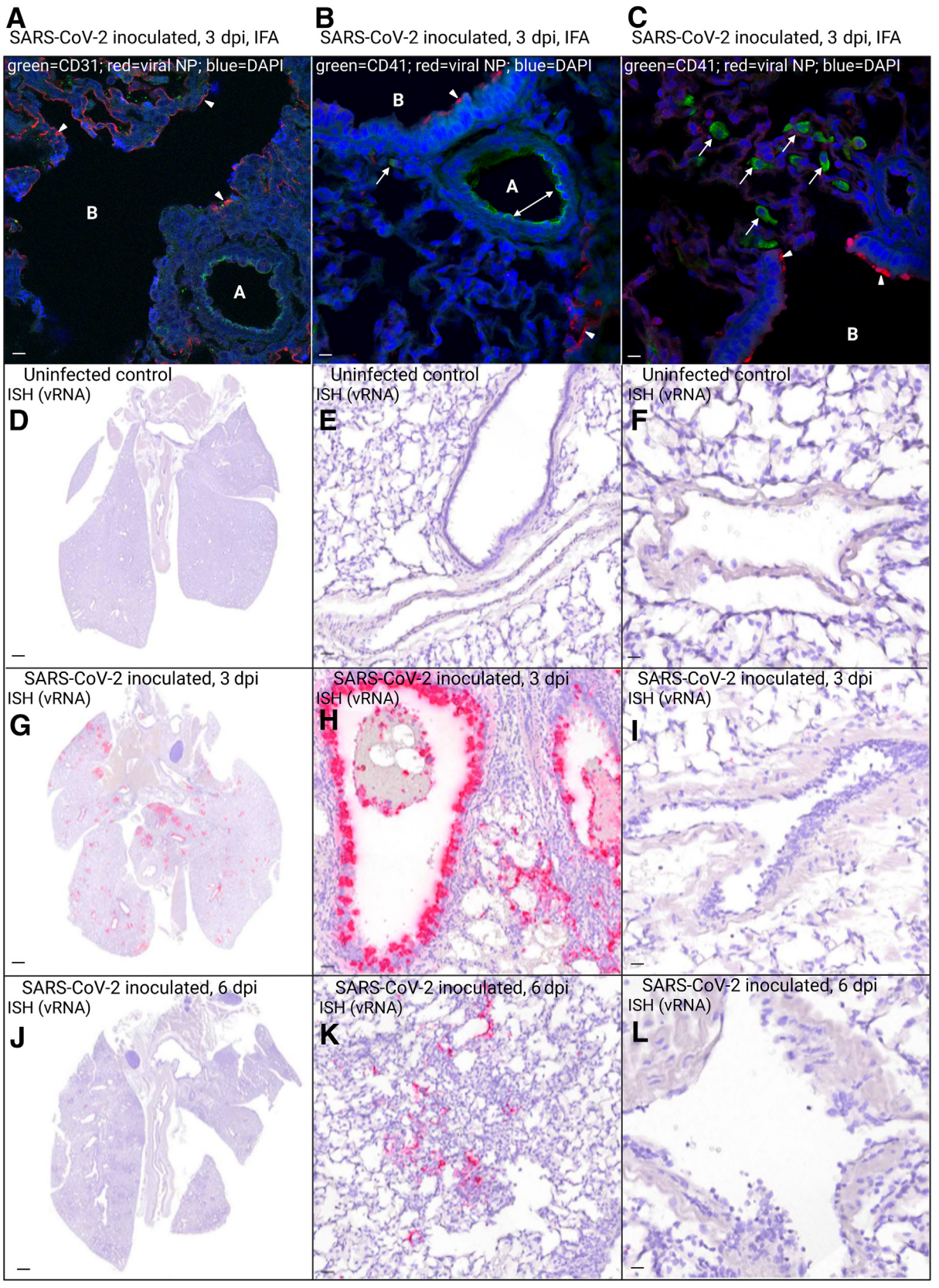
A
SARS-CoV-2 inoculated, 3 dpi, IFA
green=CD31; red=viral NP; blue=DAPI
B
C
SARS-CoV-2 inoculated, 3 dpi, IFA
green=CD41; red=viral NP; blue=DAPI
SARS-CoV-2 inoculated, 3 dpi, IFA
green=CD41; red=viral NP; blue=DAPI
Uninfected control
ISH (vRNA)
D
Uninfected control
ISH (vRNA)
E
Uninfected control
ISH (vRNA)
F
SARS-CoV-2 inoculated, 3 dpi
ISH (vRNA)
G
SARS-CoV-2 inoculated, 3 dpi
ISH (vRNA)
H
SARS-CoV-2 inoculated, 3 dpi
ISH (vRNA)
I
SARS-CoV-2 inoculated, 6 dpi
ISH (vRNA)
J
SARS-CoV-2 inoculated, 6 dpi
ISH (vRNA)
K
SARS-CoV-2 inoculated, 6 dpi
ISH (vRNA)
L

vasculitis with microthrombi (also frequently reported in humans) were not significant features in these hamsters. This disparity may reflect the timing of disease progression, the presence of comorbidities, and/or other host-specific factors. *In vivo* hamster studies employ healthy animals and are terminated by 10 to 14 dpi.[6–9] In contrast, human autopsy data largely derive from hospitalized patients with severe COVID-19 exacerbated by comorbidities and extensive exposure to medications, with a median duration between symptom onset and death exceeding 15 days.[20,21] Supporting this hypothesis, lung specimens from two patients with pulmonary adenocarcinoma retrospectively diagnosed with SARS-CoV-2 infection also lacked hyaline membranes and microthrombi, presumably because COVID-19 was an unexpected, ancillary diagnosis and the lobectomies happened to capture the acute stage of disease.[19]

TEM and special staining techniques demonstrated that endotheliitis in SARS-CoV-2–inoculated hamsters is associated with endothelial cell damage, characterized by marked cytoplasmic vacuolation with thickened irregular basement membranes, platelet marginalization, and infiltration of macrophages. In contrast, previously documented cases of non–COVID-19–associated endotheliitis, including hepatic sinusoidal endotheliitis associated with acute cellular rejection of liver allografts[1] and corneal endotheliitis secondary to herpes viral infection or corneal graft rejection,[22] tend to be lymphocytic in nature. These findings are consistent with published data; Allnoch et al[23] recently reported similar histopathologic, immunohistochemical, and ultrastructural findings in SARS-CoV-2–inoculated Syrian golden hamsters.

Both direct and indirect mechanisms of endothelial damage have been implicated in the pathogenesis of COVID-19–induced vasculopathy.[3,5] *In vitro* studies have identified viral antigen and/or RNA within endothelial cells,[24,25] particularly senescent endothelial cells.[25] In autopsy tissues, virus-like particles have been identified ultrastructurally within endothelial cells.[2,26–29] Notably, studies utilizing molecular techniques to identify endothelial viral antigen or RNA[2,30] generally fail to exclude staining of vascular support cells, such as pericytes and vascular smooth muscle cells, which are closely associated with the endothelium and express the SARS-CoV-2 receptor angiotensin-converting enzyme 2.[31–33] Overall, attempts to localize viral antigen/RNA to endothelial cells have been largely unsuccessful, equivocal,[26,28,34–37] or only possible at early time points, where it associates with a lack of viral replication or endothelial damage.[25] Additional studies report that endothelial cells do not express high levels of angiotensin-converting enzyme 2 and that they are capable of only low levels of viral replication, even when exposed to high titers of SARS-CoV-2.[33,38] Furthermore, the ultrastructural studies described above are underlined by a collective lack of reproducibility,[39] and critics have suggested that some of the viral particles reported in the literature may actually be subcellular organelles, such as coated vesicles.[40,41] Perturbations of vascular support cells may also contribute to COVID-19–associated coagulopathy, as *in vitro* exposure of human pericytes to SARS-CoV-2 spike protein resulted in dysfunctional pericyte signaling, secretion of proinflammatory cytokines, and endothelial cell death.[31,32] Together, these data and ours support an indirect mechanism of SARS-CoV-2–induced vascular damage in hamsters.

Although the pathogenesis of SARS-CoV-2–induced vascular damage has yet to be defined, existing data suggest that dysregulation of the systemic immune response may play a significant role. Systemic inflammation generates cross talk between platelets, endothelial cells, and leukocytes, ultimately resulting in endothelial damage, platelet hyperactivation, parallel activation of the coagulation cascade, and thrombosis.[42] The so-called cytokine storm[5,43] produces a self-amplifying loop, where activated endothelial cells promote leukocyte and platelet adherence, microvascular obstruction, extensive vascular inflammation, and subsequent production and release of toxic reactive oxygen species and proinflammatory cytokines, including IL-6, IL-1β (a key cytokine associated with endothelial dysfunction), and tumor necrosis factor-α. Rodent models of pulmonary infection/inflammation (including SARS-CoV-2) have demonstrated a correlation between increased proinflammatory mediators and decreased aquaporins (which are transmembrane proteins important in paracellular fluid exchange), leading to postulation that pulmonary vascular alterations and perivascular edema may result in loss of

Figure 3 Photomicrographs of immunofluorescence (IFA) antibody– and *in situ* hybridization (ISH)–labeled sections of lung from uninfected and SARS-CoV-2–inoculated hamsters. **A–C:** IFA with antibodies against SARS-CoV-2 nucleocapsid protein (NP; red) at 3 days post inoculation (dpi) shows the presence of viral antigen (**arrowheads**) within hamster terminal bronchiolar epithelium (**A–C**), alveolar septa (**B**), and, less commonly, alveolar macrophages (**B** and **C**). **A:** Anti–endothelial cell antibody CD31 (green) highlights endothelial cells lining a small pulmonary artery, which lacks red SARS-CoV-2 NP signal. **B** and **C:** Anti-platelet antibody CD41 (green) highlights platelet marginalization along the arteriolar endothelium (**double-headed arrow**; **B**), and the presence of intracytoplasmic green signal within mononuclear cells (**B** and **C**) is consistent with platelet phagocytosis by alveolar macrophages (**arrows**). **A–C:** Viral NP is not associated with pulmonary vessels. **D–L:** Distribution of SARS-CoV-2 RNA-positive cells in ISH-labeled sections of lung. Cells labeled by riboprobe *in situ* hybridization stain red. **D–F:** Lung from uninfected hamster is negative for ISH signal. **G** and **H:** In lung sections from a SARS-CoV-2–inoculated hamster euthanized at 3 dpi, SARS-CoV-2 RNA is most prominent within airways, extending from mainstem bronchi to bronchiolar epithelial cells of smaller airways and multifocally into type I and II pneumocytes of peribronchiolar alveolar septa. **J** and **K:** In lung sections from a SARS-CoV-2–inoculated hamster euthanized at 6 dpi, the number of positive cells has decreased dramatically, with scattered signal in pneumocytes lining alveolar septa, and occasional weak signal remaining in airway epithelial cells. **F**, **I**, and **L:** No signal is identified within pulmonary vessels. DAPI binds DNA. Scale bars: 20 μm (**A–C**, **E**, **F**, **H**, **I**, **K**, and **L**); 1 mm (**D**, **G**, and **J**). A, arteriole; B, bronchiole; vRNA, viral RNA.

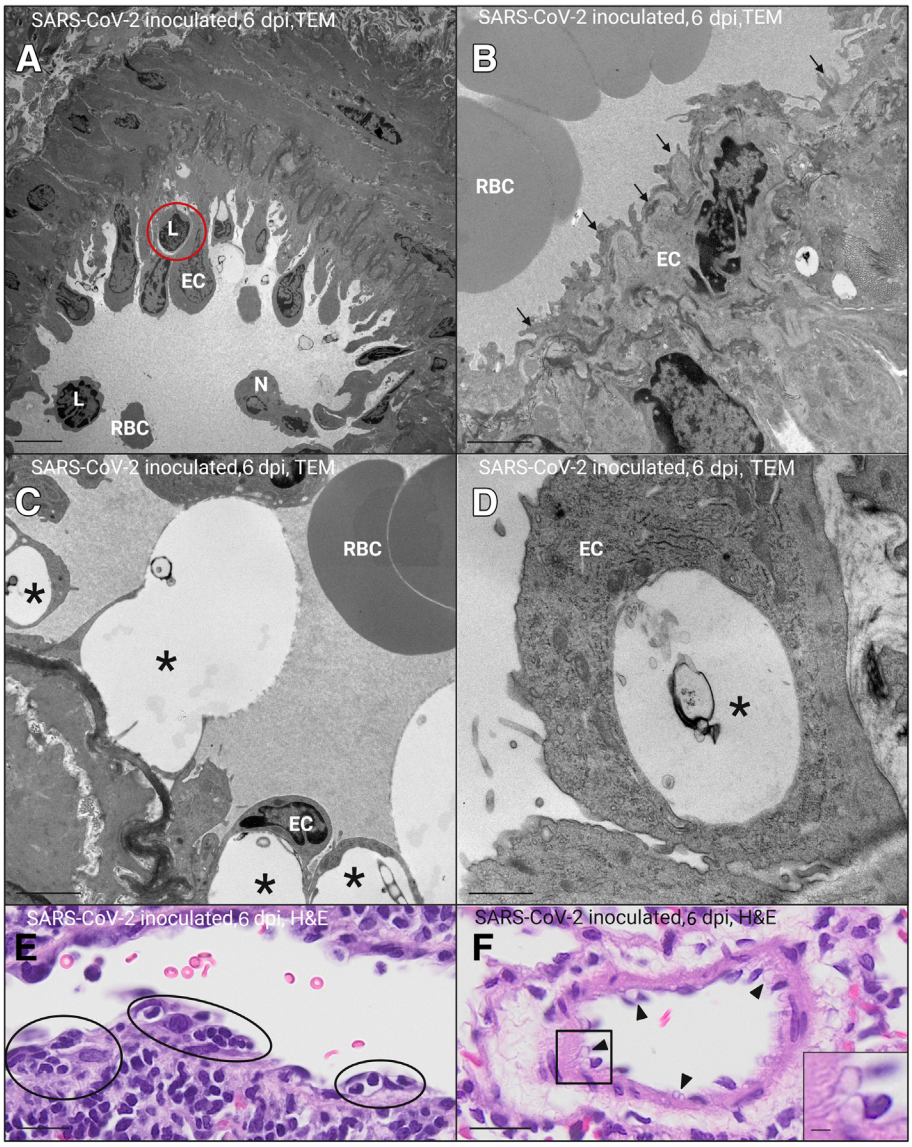

Figure 4 Transmission electron microscopic (TEM) and corresponding light-microscopic images of hamster pulmonary blood vessels 6 days after inoculation (dpi) with SARS-CoV-2. **A**—**D:** TEM images. **E** and **F:** Hematoxylin and eosin (H&E)—stained light microscopic images corresponding with TEM images. **A:** Activated endothelial cells (ECs) lining a small pulmonary arteriole and bulging into the vascular lumen with a subintimal lymphocyte (L; red circle). **B:** Activated venular endothelial cell with frond-like filopodia (**arrows**). **C** and **D:** Damaged, degenerating endothelial cells with marked cytoplasmic vacuolation (**asterisks**; **C** and **D**), resulting in partial detachment from the underlying, thickened basal lamina (**C**). **E:** Small pulmonary arteriole exhibiting endothelial bulging into the lumen with subintimal infiltration of mononuclear cells (black circles; corresponds with **A**). **F:** Endothelial cell cytoplasmic vacuolation (**black arrowheads**; corresponding with **C** and **D**). **F: Inset:** Higher-magnification view of endothelial cytoplasmic vacuolation (from **black boxed area**). Scale bars: 5 μm (**A**); 2 μm (**B**, **C**, and **F, inset**); 1 μm (**D**); 20 μm (**E** and **F**, **main image**). N, neutrophil; RBC, red blood cell.

endothelial cell integrity and loosening of intercellular junctions.[23,44] The end result of these dynamic, multifaceted, and often overlapping processes is a procoagulant, proinflammatory state characterized by increased vascular permeability, further production of proinflammatory cytokines and coagulation factors, and activation of platelets and leukocytes.[45] Activated platelets release vasoactive, hemostatic, and inflammatory mediators, trigger the coagulation cascade, and provide a procoagulant surface for secondary hemostasis,[46,47] exacerbating the existing inflammatory milieu and generating a hypercoagulable state and clinical signs of impaired coagulation.

In addition, high levels of complement component C3a in patients with severe COVID-19 are associated with differentiation/degranulation of cytotoxic T cells and subsequent endothelial injury.[48] Cytokines (eg, IL-8), complement components (eg, C5a), and activated platelets can additionally induce release of neutrophil extracellular traps (NETs), scaffolds of extracellular DNA with attached histones, neutrophil granule proteins, and antimicrobial

peptides that function to trap, immobilize, and/or kill pathogens[5,49,50] and are also known to induce the formation of immunologically mediated microthrombi (immunothrombosis).[49] Notably, Becker et al[11] recently demonstrated the presence of NETosis markers, but not viral antigen, associated with microscopic vascular lesions in a hamster model of COVID-19. A human cohort study similarly reported elevated serum markers for NETosis, microscopic evidence of extensive neutrophil-platelet infiltration, and NET-containing pulmonary microthrombi in patients with severe COVID-19.[49] This precarious clinical situation is exacerbated by both aging and preexisting cardiovascular risk factors, such as obesity, hypertension, and diabetes,[5] which are also known to prime platelets for hyperreactivity.[46]

Immune dysregulation, resulting in excessive production of proinflammatory cytokines, endothelial damage, and platelet hyperactivation, is a plausible driving force behind the hypercoagulable state and microthrombosis observed in some patients with COVID-19. Although this was an observational study, these findings, particularly the lack of viral association with inflamed vessels, and published data[5,11,30,46,51–53] collectively support a primarily indirect mechanism linking inflammation and hypercoagulability in severe cases of COVID-19. Although further study regarding viral effects on pericytes and endothelium-platelet-leukocyte interactions is necessary to fully understand the pathogenesis of SARS-CoV-2–associated coagulopathy, our results suggest that novel therapeutics targeting the dysregulated immune system (ie, cytokine production or NETosis) may prove to be effective medical countermeasures against COVID-19. To our knowledge, this is the first use of TEM and special histologic staining techniques to demonstrate endothelial damage with marginalization of activated platelets and lack of viral association with affected blood vessels in regions of active pulmonary SARS-CoV-2 infection in a Syrian golden hamster model of human COVID-19.

Acknowledgments

We thank Bradley Shibata for assistance with transmission electron microscopy; Zhong Min-Ma for assistance with *in situ* hybridization; and the pathology staff (University of California, Davis, School of Veterinary Medicine).

Supplemental Data

Supplemental material for this article can be found at *http://doi.org/10.1016/j.ajpath.2023.02.013*.

References

1. Shi Y, Dong K, Zhang YG, Michel RP, Marcus V, Wang YY, Chen Y, Gao ZH: Sinusoid endotheliitis as a histological parameter for diagnosing acute liver allograft rejection. World J Gastroenterol 2017, 23:792–799
2. Ackermann M, Verleden SE, Kuehnel M, Haverich A, Welte T, Laenger F, Vanstapel A, Werlein C, Stark H, Tzankov A, Li WW, Li VW, Mentzer SJ, Jonigk D: Pulmonary vascular endothelialitis, thrombosis, and angiogenesis in Covid-19. N Engl J Med 2020, 383: 120–128
3. Colling ME, Kanthi Y: COVID–19-associated coagulopathy: an exploration of mechanisms. Vasc Med 2020, 25:471–478
4. Panigada M, Bottino N, Tagliabue P, Grasselli G, Novembrino C, Chantarangkul V, Pesenti A, Peyvandi F, Tripodi A: Hypercoagulability of COVID-19 patients in intensive care unit: a report of thromboelastography findings and other parameters of hemostasis. J Thromb Haemost 2020, 18:1738–1742
5. Gu SX, Tyagi T, Jain K, Gu VW, Lee SH, Hwa JM, Kwan JenniferM, Krause DS, Lee AI, Halene S, Martin KA, Chun HJ, Hwa J: Thrombocytopathy and endotheliopathy: crucial contributors to COVID-19 thromboinflammation. Nat Rev Cardiol 2021, 18: 194–209
6. Imai M, Iwatsuki-Horimoto K, Hatta M, Loeber S, Halfmann PJ, Nakajima N, Watanabe T, Ujie M, Takahashi K, Ito M, Yamada S, Fan S, Chiba S, Kuroda M, Guan L, Takada K, Armbrust T, Balogh A, Furusawa Y, Okuda M, Ueki H, Yasuhara A, Sakai-Tagawa Y, Lopes, Tiago JS, Kiso M, Yamayoshi S, Kinoshita N, Ohmagari N, Hattori SI, Takeda M, Mitsuya H, Krammer F, Suzuki T, Kawaoka Y: Syrian hamsters as a small animal model for SARS-CoV-2 infection and countermeasure development. Proc Natl Acad Sci U S A 2020, 117:16587–16595
7. Chan JFW, Zhang AJ, Yuan S, Poon VKM, Chan CCS, Lee ACY, Chan, Wan Mui, Fan Z, Tsoi HW, Wen L, Liang R, Cao J, Chen Y, Tang K, Luo C, Cai JP, Kok KH, Chu H, Chan KH, Sridhar S, Chen Z, Chen H, To KKW, Yuen KY: Simulation of the clinical and pathological manifestations of coronavirus disease 2019 (COVID-19) in a golden Syrian hamster model: implications for disease pathogenesis and transmissibility. Clin Infect Dis 2020, 71:2428–2446
8. Roberts A, Vogel L, Guarner J, Hayes N, Murphy B, Zaki S, Subbarao K: Severe acute respiratory syndrome coronavirus infection of golden Syrian hamsters. J Virol 2005, 79:503–511
9. Sia SF, Yan LM, Chin AWH, Fung K, Choy KT, Wong AYL, Kaewpreedee P, Perera RAPM, Poon LLM, Nicholls JM, Peiris M, Yen HL: Pathogenesis and transmission of SARS-CoV-2 in golden hamsters. Nature 2020, 583:834–838
10. Mulka KR, Beck SE, Solis CV, Johanson AL, Queen SE, McCarron ME, et al: Progression and resolution of severe acute respiratory syndrome coronavirus 2 (SARS-CoV-2) infection in golden Syrian hamsters. Am J Pathol 2022, 192:195–207
11. Becker K, Beythien G, de Buhr N, Stanelle-Bertram S, Tuku B, Kouassi NM, Beck S, Zickler M, Allnoch L, Gabriel G, von Köckritz-Blickwede M, Baumgärtner W: Vasculitis and neutrophil extracellular traps in lungs of golden Syrian hamsters with SARS-CoV-2. Front Immunol 2021, 12:1–11
12. Committee for the Update of the Guide for the Care and Use of Laboratory Animals; National Research Council: Guide for the Care and Use of Laboratory Animals. Eighth Edition. Washington, DC, National Academies Press, 2011
13. Rosenke K, Meade-White K, Letko M, Clancy C, Hansen F, Liu Y, Okumura A, Tang-Huau TS, Li R, Saturday G, Feldmann F, Scott D, Wang Z, Munster V, Jarvis MA, Feldmann H: Defining the Syrian hamster as a highly susceptible preclinical model for SARS-CoV-2 infection. Emerg Microbes Infect 2020, 9:2673–2684
14. Song Z, Bao L, Yu P, Qi F, Gong S, Wang J, Zhao B, Liu M, Han Y, Deng W, Liu J, Wei Q, Xue J, Zhao W, Qin C: SARS-CoV-2 causes a systemically multiple organs damages and dissemination in hamsters. Front Microbiol 2021, 11:1–15
15. Carroll T, Fox D, van Doremalen N, Ball E, Morris MK, Sotomayor-Gonzalez A, Servellita V, Rustagi A, Yinda CK, Fritts L, Port JR, Ma ZM, Holbrook MG, Schulz J, Blish CA, Hanson C, Chiu CY

Munster V, Stanley S, Miller CJ: The B.1.427/1.429 (epsilon) SARS-CoV-2 variants are more virulent than ancestral B.1 (614G) in Syrian hamsters. PLoS Pathog 2022, 18:1−24
16. Saito A, Irie T, Suzuki R, Maemura T, Nasser H, Uriu K, et al: Enhanced fusogenicity and pathogenicity of SARS-CoV-2 Delta P681R mutation. Nature 2021, 602:300−306
17. Buja LM, Wolf D, Zhao B, Akkanti B, McDonald M, Lelenwa L, Reilly N, Ottaviani G, Elghetany MT, Trujillo DO, Aisenberg GM, Madjid M, Kar B: The emerging spectrum of cardiopulmonary pathology of the coronavirus disease 2019 (COVID-19): report of 3 autopsies from Houston, Texas, and review of autopsy findings from other United States cities. Cardiovasc Pathol 2020, 48:107233
18. Carsana L, Sonzogni A, Nasr A, Rossi RS, Pellegrinelli A, Zerbi P, Rech R, Colombo R, Antinori S, Corbellino M, Galli M, Catena E, Tosoni A, Gianatti A, Nebuloni M: Pulmonary post-mortem findings in a series of COVID-19 cases from Northern Italy: a two-centre descriptive study. Lancet Infect Dis 2020, 20:1135−1140
19. Tian S, Hu W, Niu L, Liu H, Xu H, Xiao SY: Pulmonary pathology of early-phase 2019 novel coronavirus (COVID-19) pneumonia in two patients with lung cancer. J Thorac Oncol 2020, 15:700−704
20. de Roquetaillade C, Bredin S, Lascarrou JB, Soumagne T, Cojocaru M, Chousterman BG, Leclerc M, Gouhier A, Piton G, Pène F, Stoclin A, Llitjos FJ: Timing and causes of death in severe COVID-19 patients. Crit Care 2021, 25:1−8
21. Faes C, Abrams S, Van Beckhoven D, Meyfroidt G, Vlieghe E, Hens N: Time between symptom onset, hospitalisation and recovery or death: statistical analysis of Belgian covid-19 patients. Int J Environ Res Public Health 2020, 17:1−18
22. Ding K, Nataneli N: Cytomegalovirus Corneal Endotheliitis. Treasure Island, FL, StatPearls Publishing, 2022
23. Allnoch L, Beythien G, Leitzen E, Becker K, Kaup FJ, Stanelle-Bertram S, Schaumburg B, Mounogou Kouassi N, Beck S, Zickler M, Herder V, Gabriel G, Baumgärtner W: Vascular inflammation is associated with loss of aquaporin 1 expression on endothelial cells and increased fluid leakage in sars-cov-2 infected golden Syrian hamsters. Viruses 2021, 13:1−18
24. Monteil V, Kwon H, Prado P, Hagelkrüys A, Wimmer RA, Stahl M, Leopoldi A, Garreta E, Hurtado del Pozo C, Prosper F, Romero JP, Wirnsberger G, Zhang H, Slutsky AS, Conder R, Montserrat N, Mirazimi A, Penninger JM: Inhibition of SARS-CoV-2 Infections in engineered human tissues using clinical-grade soluble human ACE2. Cell 2020, 181:905−913.e7
25. Urata R, Ikeda K, Yamazaki E, Ueno D, Katayama A, Shin-Ya M, Ohgitani E, Mazda O, Satoaki Matoba S: Senescent endothelial cells are predisposed to SARS-CoV-2 infection and subsequent endothelial dysfunction. Sci Rep 2022, 12:1−9
26. Varga Z, Flammer AJ, Steiger P, Haberecker M, Andermatt R, Zinkernagel AS, Mehra MR, Schuepbach RA, Ruschitzka F, Moch H: Endothelial cell infection and endotheliitis in COVID-19. Lancet 2020, 395:1417−1418
27. Paniz-Mondolfi A, Bryce C, Grimes Z, Gordon RE, Reidy J, Lednicky J, Sordillo EM, Fowkes M: Central nervous system involvement by severe acute respiratory syndrome coronavirus-2 (SARS-CoV-2). J Med Virol 2020, 92:699−702
28. Bradley BT, Maioli H, Johnston R, Chaudhry I, Fink SL, Xu H, Najafian B, Deutsch G, Lacy JM, Williams T, Yarid N, Marshall DA: Histopathology and ultrastructural findings of fatal COVID-19 infections in Washington State: a case series. Lancet 2020, 396:320−332
29. Garrido Ruiz MC, Santos-Briz Á, Sánchez A, Alonso-Riaño M, Burgos J, Medina Miguelañez M, Puebla L, Román-Curto C, Roncero-Riesco M, Garcia R, Ortiz PL, Rodriguez-Peralto JL: Spectrum of clinicopathologic findings in COVID-19-induced skin lesions: demonstration of direct viral infection of the endothelial cells. Am J Surg Pathol 2021, 45:293−303
30. Lowenstein CJ, Solomon SD: Severe COVID-19 is a microvascular disease. Circulation 2020, 142:1609−1611
31. Avolio E, Carrabba M, Milligan R, Williamson MK, Beltrami AP, Gupta K, Elvers KT, Gamez M, Foster RR, Gillespie K, Hamilton F, Arnold D, Berger I, Davidson AD, Hill D, Caputo M, Madeddu P: The SARS-CoV-2 Spike protein disrupts human cardiac pericytes function through CD147 receptor-mediated signalling: a potential non-infective mechanism of COVID-19 microvascular disease. Clin Sci 2021, 135:2667−2689
32. Khaddaj-Mallat R, Aldib N, Bernard M, Paquette AS, Ferreira A, Lecordier S, Saghatelyan A, Flamand L, ElAli A: SARS-CoV-2 deregulates the vascular and immune functions of brain pericytes via Spike protein. Neurobiol Dis 2021, 161:105561
33. He L, Mäe MA, Muhl L, Sun Y, Pietilä R, Nahar K, et al: Pericyte-specific vascular expression of SARS-CoV-2 receptor ACE2—implications for microvascular inflammation and hypercoagulopathy in COVID-19. bioRxiv 2020. [Preprint] doi: 10.1101/2020.05.11.088500
34. Schaefer IM, Padera RF, Solomon IH, Kanjilal S, Hammer MM, Hornick JL, Sholl LM: In situ detection of SARS-CoV-2 in lungs and airways of patients with COVID-19. Mod Pathol 2020, 33:2104−2114
35. Akilesh S, Nast CC, Yamashita M, Henriksen K, Charu V, Troxell ML, Kambham N, Bracamonte E, Houghton D, Ahmed NI, Chong CC, Thajudeen B, Rehman S, Khoury F, Zuckerman JE, Gitomer J, Raguram PC, Mujeeb S, Schwarze U, Shannon MB, De Castro I, Alpers CE, Najafian B, Nicosia RF, Andeen NK, Smith KD: Multicenter clinicopathologic correlation of kidney biopsies performed in COVID-19 patients presenting with acute kidney injury or proteinuria. Am J Kidney Dis 2021, 77:82−93.e1
36. Peleg Y, Kudose S, D'Agati V, Siddall E, Ahmad S, Nickolas T, Kisselev S, Gharavi A, Canetta P: Acute kidney injury due to collapsing glomerulopathy following COVID-19 infection. Kidney Int Rep 2020, 5:940−945
37. Wu H, Larsen CP, Hernandez-Arroyo CF, Mohamed MMB, Caza T, Sharshir M, Chughtai A, Xie L, Gimenez JM, Sandow TA, Lusco MA, Yang H, Acheampong E, Rosales IA, Colvin RB, Fogo AG, Velez JCQ: AKI and collapsing glomerulopathy associated with covid-19 and apol1 high-risk genotype. J Am Soc Nephrol 2020, 31:1688−1695
38. McCracken IR, Saginc G, He L, Huseynov A, Daniels A, Fletcher S, Peghaire C, Kalna V, Andaloussi-Mäe M, Muhl L, Craig NM, Griffiths SJ, Haas JG, Tait-Burkard C, Lendahl U, Birdsey GM, Betsholtz C, Noseda M, Baker AH, Randi AM: Lack of evidence of angiotensin-converting enzyme 2 expression and replicative infection by SARS-CoV-2 in human endothelial cells. Circulation 2021, 143:865−868
39. Nicosia RF, Ligresti G, Caporarello N, Akilesh S, Ribatti D: COVID-19 vasculopathy: mounting evidence for an indirect mechanism of endothelial injury. Am J Pathol 2021, 191:1374−1384
40. Goldsmith CS, Miller SE, Martines RB, Bullock HA, Zaki SR: Electron microscopy of SARS-CoV-2: a challenging task. Lancet 2020, 395:e99
41. Goldsmith CS, Tatti KM, Ksiazek TG, Rollin PE, Comer JA, Lee WW, Rota PA, Bankamp B, Bellini WJ, Zaki SR: Ultrastructural characterization of SARS coronavirus. Emerg Infect Dis 2004, 10:320−326
42. Coenen DM, Mastenbroek TG, Cosemans JMEM: Platelet interaction with activated endothelium: mechanistic insights from microfluidics. Blood 2017, 130:2819−2828
43. Fajgenbaum DC, June CH: Cytokine storm. N Engl J Med 2020, 383:2255−2273
44. Meli R, Pirozzi C, Pelagalli A: New perspectives on the potential role of aquaporins (AQPs) in the physiology of inflammation. Front Physiol 2018, 9:1−11
45. Godo S, Shimokawa H: Endothelial functions. Arterioscler Thromb Vasc Biol 2017, 37:e108−e114
46. Brambilla M, Canzano P, Becchetti A, Tremoli E, Camera M: Alterations in platelets during SARS-CoV-2 infection. Platelets 2022, 33:192−199

47. Koupenova M, Clancy L, Corkrey HA, Freedman JE: Circulating platelets as mediators of immunity, inflammation, and thrombosis. Circ Res 2018, 122:337−351
48. Georg P, Astaburuaga-García R, Bonaguro L, Brumhard S, Michalick L, Lippert LJ, et al: Complement activation induces excessive T cell cytotoxicity in severe COVID-19. Cell 2022, 185: 493−512.e25
49. Middleton EA, He XY, Denorme F, Campbell RA, Ng D, Salvatore SP, Mostyka M, Baxter-Stoltzfus A, Borczuk AC, Loda M, Cody MJ, Manne BK, Portier I, Harris ES, Petrey AC, Beswick EJ, Caulin AF, Iovino A, Abegglen LM, Weyrich AS, Rondina MT, Egeblad M, Schiffman JD, Yost CC: Neutrophil extracellular traps contribute to immunothrombosis in COVID-19 acute respiratory distress syndrome. Blood 2020, 136:1169−1179
50. Goggs R, Jeffery U, LeVine DN, Li RHL: Neutrophil-extracellular traps, cell-free DNA, and immunothrombosis in companion animals: a review. Vet Pathol 2020, 57:6−23
51. Canzano P, Brambilla M, Porro B, Cosentino N, Tortorici E, Vicini S, Poggio P, Cascella A, Pengo MF, Veglia F, Fiorelli S, Bonomi A, Cavalca V, Trabattoni D, Andreini D, Omodeo Salè E Parati G, Tremoli E, Camera M: Platelet and endothelial activation as potential mechanisms behind the thrombotic complications of COVID-19 patients. JACC Basic Transl Sci 2021, 6:202−218
52. Zaid Y, Puhm F, Allaeys I, Naya A, Oudghiri M, Khalki L, Limami Y, Zaid N, Sadki K, Ben El Haj R, Mahir W, Belayachi L, Belefquih B, Benouda A, Cheikh A, Langlois MA, Cherrah Y, Flamand L, Guessous F, Boilard E: Platelets can associate with SARS-CoV-2 RNA and are hyperactivated in COVID-19. Circ Res 2020, 127:1404−1418
53. Cappellano G, Raineri D, Rolla R, Giordano M, Puricelli C, Vilardo B, Manfredi M, Cantaluppi V, Sainaghi PP, Castello L, De Vita N, Scotti L, Vaschetto R, Dianzani U, Chiocchetti A: Communication circulating platelet-derived extracellular vesicles are a hallmark of sars-cov-2 infection. Cells 2021, 10:1−10